


Confinement effects on the mechanical heterogeneity of polymer fiber glasses

Taejin Kwon and Bong June Sung*

Department of Chemistry, Sogang University, Seoul 04107, Republic of Korea (Received 19 June 2020; revised 8 October 2020; accepted 13 October 2020; published 3 November 2020)

Both polymer fiber glasses and bulk polymer glasses exhibit nonlinear mechanical responses under uniaxial deformation. In polymer fibers, however, polymer chains are confined strongly and the surface area is relatively large compared to their volume. The confinement and the surface may lead to the spatially heterogeneous relaxation of chains in polymer fibers. In this work we perform molecular dynamics simulations and investigate the relation between the heterogeneous dynamics and the nonlinear mechanical responses at a molecular level. Our molecular simulations capture successfully not only the nonlinear mechanical response but also the dependence of mechanical properties on the strain rate of typical polymer glasses as in experiments. We find that the local elastic modulus and the nonaffine displacement are spatially heterogeneous in the pre-yield regime, which results in a lower elastic modulus for polymer fibers than bulk polymer glasses. In the post-yield regime, those mechanical properties become relatively homogeneous. Monomers with large nonaffine displacement are localized mainly at the interfacial region in the pre-yield regime while highly nonaffine monomers are distributed throughout the fibers in the post-yield regime. We show that the nonaffine displacement during deformation relates closely to the mechanical response of the polymer fibers. We also find that in the strain-hardening regime there is a significant difference in the energetic contribution to the stress between polymer fibers and bulk polymers, for which the modulus of the strain-hardening regime of the polymer fibers is smaller than that of bulk polymers.

DOI: [10.1103/PhysRevE.102.052501](https://doi.org/10.1103/PhysRevE.102.052501)

I. INTRODUCTION

The relaxation dynamics and the glass transition of confined polymers (such as polymer films and polymer fibers) are different from those of bulk polymers. For example, Forrest *et al.* [1] showed that the glass transition temperature (T_g) of free-standing polystyrene (PS) thin films depended on the film thickness (unlike bulk polymer melts) and decreased by about 20% with a decrease in the film thickness from 180 to 29 nm. The presence of considerably large interfacial regions in confined polymers could make the relaxation dynamics spatially heterogeneous, which have been discussed in experiments and theoretical studies extensively [1–6]. Heterogeneous relaxation dynamics is of crucial importance in understanding complicated mechanical properties of the confined polymer glasses [7–9]. However, the relationship between the dynamic heterogeneity and the macroscopic mechanical response of confined polymers still remains unclear. In this work, therefore, we perform molecular dynamics simulations and investigate the effects of the confinement and the surface of polymer fiber glasses under large deformation.

Polymer (nano)fiber glasses with diameters from 10 to 600 nm have drawn attention due to its wide applicability for tissue engineering [10–12], drug delivery systems [13–15], composites materials [16–18], and energy storage systems [19–21]. Not surprisingly, it is a fundamental issue in those applications to control the mechanical properties of polymer

fibers. Recent experiments and simulation studies revealed that the mechanical properties were determined by various factors including entanglement [22], confinement effects [23], crystallinity [24], chain orientation [25], and chain flexibility [26]. Such various factors make it difficult to obtain general insights on the mechanical properties from previous studies. For example, Arinstein *et al.* [23] showed that the Young's modulus of nylon 6,6 nanofibers increased by three times with a decrease in the diameter from 900 to 400 nm. On the other hand, Buell *et al.* [27] carried out extensive molecular dynamic simulations of glassy polyethylene (PE) nanofibers, and showed that Young's modulus decreased by about 30% with a decrease in the fiber diameter from 17.7 to 3.7 nm. In order to elucidate the effect of the interfacial region and the confinement systematically, therefore, one may take advantage of a generic model. The coarse-grained bead spring model has been employed extensively to investigate the relaxation dynamics and the mechanical responses of polymeric glasses [28–30]. For example, a simulation study with the bead spring model reproduced the mechanical features of PMMA glasses during the multistep creep experiments successfully [31]. Another simulation study also employed the bead spring model and predicted that strain hardening was associated closely with plastic flow [32], which was supported by a recent experiment [33]. In this study we employ a generic coarse-grained bead spring model for a polymer chain and perform systematic molecular dynamics simulations for the mechanical response of the polymer fibers.

The segmental relaxation of polymer chains is spatially heterogeneous in confined polymer glasses due to the

*bjsung@sogang.ac.kr

presence of the surface [34,35]. Paeng *et al.* [34] measured the reorientation of fluorescence probes in free-standing polystyrene (PS) films and showed that the segmental mobility in the interfacial layer was faster by four orders of magnitude than that of the bulk layer. Previous studies also showed that the modified segmental relaxation near the surface should affect T_g [36–39] and the elastic modulus [23,27,40–43]. For example, Camposeo *et al.* [44] measured and reported the local Young’s modulus of MEH-PPV fibers via AFM indentation technique. They found that the local Young’s modulus of the core region was two times larger than that of the interfacial region. It still remains unclear, however, how the segmental relaxation of chains may relate to nonlinear mechanical responses of confined polymer glasses under deformation. Therefore, we try to investigate the segmental relaxation of confined polymers during the deformation in our simulations.

The mechanical response of polymer glasses depends on the timescale of deformation [45–50]. Polymer glasses behave as elastic solids at short timescales, whereas polymer glasses act as viscous liquids at long timescales. Such viscoelasticity of polymers is responsible for the nonlinear nature of the mechanical response. For example, the stress-strain curve of polymer glasses in constant strain rate experiments exhibited nonlinear mechanical response. At quite small strains, stress increases linearly with strain (*the elastic regime*). After the elastic regime, the stress reaches a stress maximum followed by the strain softening with a drop in the stress (*the stress overshoot regime*). As the strain increases further, the stress reaches a plateau with a constant stress value (*the steady-state regime*). In cases of typical polymer glasses, stress begins to increase again, which is called *the strain hardening regime*. Previous studies revealed that such nonlinear mechanical response of polymer glasses to the deformation should relate to the segmental relaxation and its heterogeneity of polymer chains [35,51–60]. The extent of heterogeneity of segmental relaxation in polymer glasses depends on strain [31,42,61–64]. For example, Riggleman *et al.* [31] showed that in the elastic regime the extent of heterogeneity of segmental relaxation increased. But, after the elastic regime, the extent of heterogeneity of segmental relaxation decreased.

Theoretical approaches have been developed to describe the mechanical responses of polymer glasses during deformation. Eyring proposed a phenomenological description of stress-induced molecular motion where the applied stress lowered the energy barriers for molecular motions [65]. The Eyring model does not, however, predict the nonlinear mechanical response successfully beyond yield stress [31,61,66]. In order to overcome the limitation of the Eyring model, several theories have been suggested. As an example, the shear-transformation-zone (STZ) theory is a phenomenological description for the plasticity of amorphous solids and has been used widely to describe the strain softening phenomenon [67–69]. Chen and Schweizer [70–73] also proposed the excellent nonlinear Langevin equation (NLE) theory for the nonlinear mechanical response of deformed polymer glasses based on a mean-field approach. Hoy *et al.* showed that the strain hardening at large strains resulted from dissipative stress regardless of the presence of entanglement [74,75]. Even though previous theories provided systematic approaches to elucidate the nonlinear mechanical response,

mean-field theories would still lack a description for dynamic heterogeneity. It would be, therefore, of academic importance to test whether theoretical models can capture the relationship between heterogenous segmental relaxation and mechanical properties of confined polymer glasses.

In this study we employ a generic coarse-grained model for polymer chains and perform molecular dynamics simulations to investigate the nonlinear mechanical response of the glass polymer fibers. We find that our simulations reproduce the four regimes well as observed in experiments for the uniaxial deformation of glass polymer fibers. The mechanical properties such as the elastic modulus (of the elastic regime) and the strain hardening modulus (of the strain hardening regime) are dependent on the strain rate and are different from those of bulk polymer glasses. The mechanical properties are quite heterogeneous at the pre-yield regime but becomes relatively homogeneous at the post-yield regime. Such *mechanical heterogeneity* should be responsible for the difference in the elastic modulus between glass polymer fibers and bulk polymer glasses. We also find that the nonaffine displacement of monomers in the interfacial regions is larger than those in the core region of fibers. As the strain increases, however, the distribution of the nonaffine displacement becomes homogeneous in fibers.

The rest of the paper is organized as follows. We describe the simulation model and methods in Sec. II. In Sec. III, we present the simulation results and discussions, and in Sec. IV we summarize and conclude our study.

II. SIMULATION MODEL AND METHODS

We perform molecular dynamics (MD) simulations with a generic coarse-grained model for polymers. Polymer chains are modeled as bead spring chains of $N_{\text{mon}} = 32$ monomers. The number (N_{pol}) of polymers is 350 in our simulations. The nonbonding interactions [$U_{\text{nb}}(r)$] between a pair of nonbonded monomers is described via truncated and shifted Lennard-Jones (LJ) potential with a cutoff length of $r_c = 2.5\sigma$, i.e.,

$$U_{\text{nb}}(r) = \begin{cases} 4\epsilon \left[\left(\frac{\sigma}{r} \right)^{12} - \left(\frac{\sigma}{r} \right)^6 \right] - U_c, & r \leq r_c, \\ 0, & r > r_c, \end{cases} \quad (1)$$

where $U_c = 4\epsilon \left[\left(\frac{\sigma}{r_c} \right)^{12} - \left(\frac{\sigma}{r_c} \right)^6 \right]$. ϵ and σ denote the units of energy and length, respectively. r is the distance between two monomers. The bonding between two chemically bonded monomers of a chain is described by a harmonic potential, i.e., $U_b(r) = K_b(r - r_0)^2$ with $K_b = 1000\epsilon/\sigma^2$ and $r_0 = 1\sigma$. This model prevents crystallization due to the mismatch between the positions of minima of U_{nb} and U_b . The mass of a monomer (m_{mon}) is set to unity. Then, the units of the temperature (T) and the time (τ) in our simulations are reduced LJ units. All simulations are performed using LAMMPS simulation package [76]. We employ the velocity-Verlet integrator with a time step of 0.002τ .

We obtain the equilibrium configurations of a polymer fiber as follows. First, we place $N_{\text{pol}} = 350$ polymer chains at random positions in a rectangular simulation box with periodic boundary conditions applied in all directions. If there is any overlap between particles, the chains are discarded and re-inserted at different random positions. The

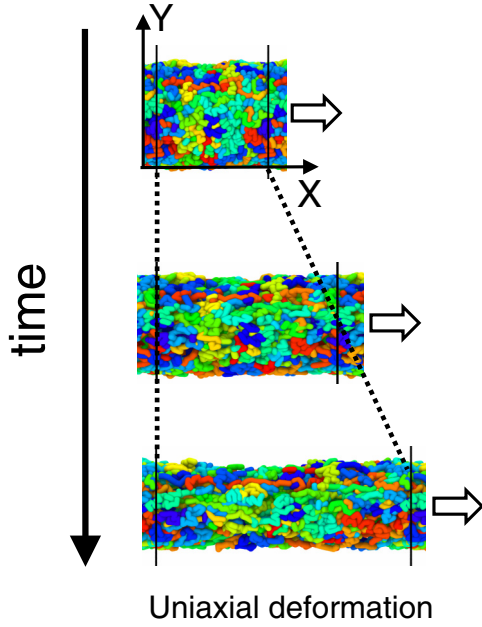


FIG. 1. Simulation snapshots of polymer fiber glasses during uniaxial deformation. Periodic boundary images along x axis are also shown. Black solid lines represent the boundaries of the primary simulation cell. The strain (γ) of each snapshot corresponds to $\gamma = 0$ (top), 0.4 (middle), and 0.8 (bottom).

dimensions of the rectangular simulation box are $(L_x, L_y, L_z) = (25\sigma, 21.166\sigma, 21.166\sigma)$ such that the number density of monomers is about 1. Once we obtain initial configurations in the rectangular simulation cell, we increase the values of both L_y and L_z to 100σ in order to construct a polymer fiber. The periodic images of a polymer chain along y and z directions cannot interact with one another (Fig. 1). Then we conduct molecular dynamics simulations until the time correlation function of the end-to-end vector of the chains decays to e^{-1} in order to equilibrate the polymer fibers. In this equilibration all simulations are performed for the canonical NVT ensemble at $T = 1$ with the Nosé-Hoover thermostat. In this work we obtain nine independent initial configurations for polymer fibers of each condition. All the properties reported in this study are averaged over nine independent trajectories. Error bars in our results are the standard errors on the mean.

After equilibration steps at $T = 1$, we cool down all systems to $T = 0.1$ in the NVT ensemble at a cooling rate (Γ) of $\Gamma = 1 \times 10^{-4}$, 1×10^{-5} , and 1×10^{-6} . Γ in this study is much faster than cooling rates used in experiments such that some properties of glassy materials may depend on cooling rates. However, note that the cooling rate in this study is comparable with the typical cooling rates used in previous simulation studies of polymeric glasses [31,49]. And we also expect that mechanical properties in our simulations can be comparable with those in experiments at least qualitatively. Unless otherwise noted, we provide the mechanical properties of polymer fibers and bulk glasses at $\Gamma = 1 \times 10^{-5}$. Upon cooling, the temperature dependence of the potential energy of systems changes before and after the glass state [Fig. 2(a)]. We estimate the glass transition temperature (T_g) of all systems by

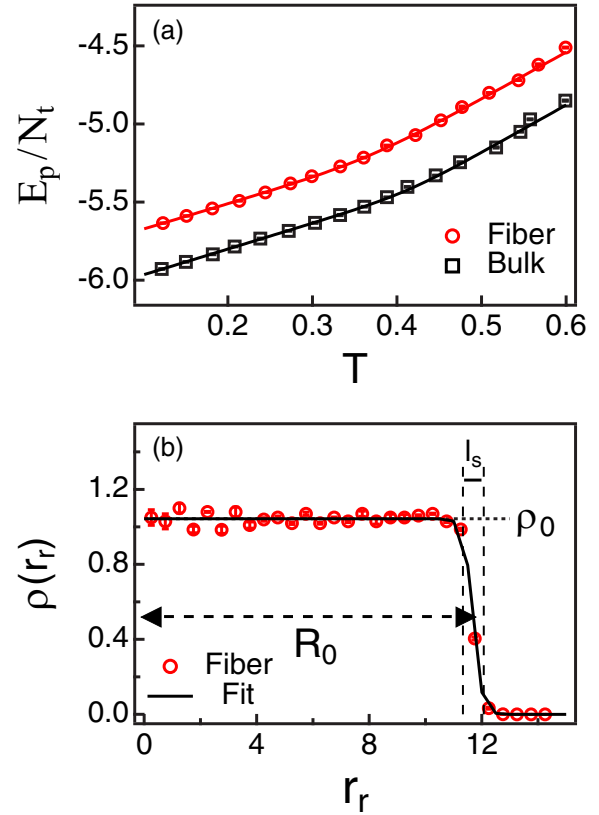


FIG. 2. (a) The temperature dependence of potential energy per particle (E_p/N_t) for polymer fibers (red) and bulk polymer melts (black). Lines are fits to the simulation results based on Eq. (2). (b) The radial density profile [$\rho(r_r)$] of polymer fiber glasses at $T = 0.1$. The black solid line is a fit based on the hyperbolic tangent equation to the simulation results (red circles). Both results are obtained at $\Gamma = 1 \times 10^{-5}$.

fitting Eq. (2) to the potential energy per particle as a function of temperature, as employed in previous studies [49,77,78]

$$E_{\text{pot}}(T)/N_t = w \left(\frac{G - M}{2} \right) \ln \left[\cosh \left(\frac{T - T_g}{w} \right) \right] + (T - T_g) \left(\frac{M + G}{2} \right) + C, \quad (2)$$

where $E_{\text{pot}}(T)$ denotes the potential energy of the system as a function of temperature T , N_t is the total number of monomers in the systems ($N_t = N_{\text{pol}} \times N_{\text{mon}}$), and M and G are the linear thermal expansion coefficients of the melt and glass, respectively. w denotes the width of the transition, and C is the potential energy per particles at $T = T_g$. We find from our simulations that $T_g = 0.36$ for glass polymer fibers. Therefore, the lowest temperature of $T = 0.1$ in our study is much lower than T_g .

We estimate the radius (R_0) of polymer fibers at $T = 0.1$ by calculating the radial density profile $\rho(r_r)$ as follows:

$$\rho(r_r) \equiv \left\langle \frac{1}{N_t} \sum_{i=1}^{N_t} \frac{1}{2\pi r_r} \delta(r_r - r_i) \right\rangle, \quad (3)$$

where i denotes the monomer index, and r_r is the shortest distance from the central axis of the fiber. r_i is the shortest

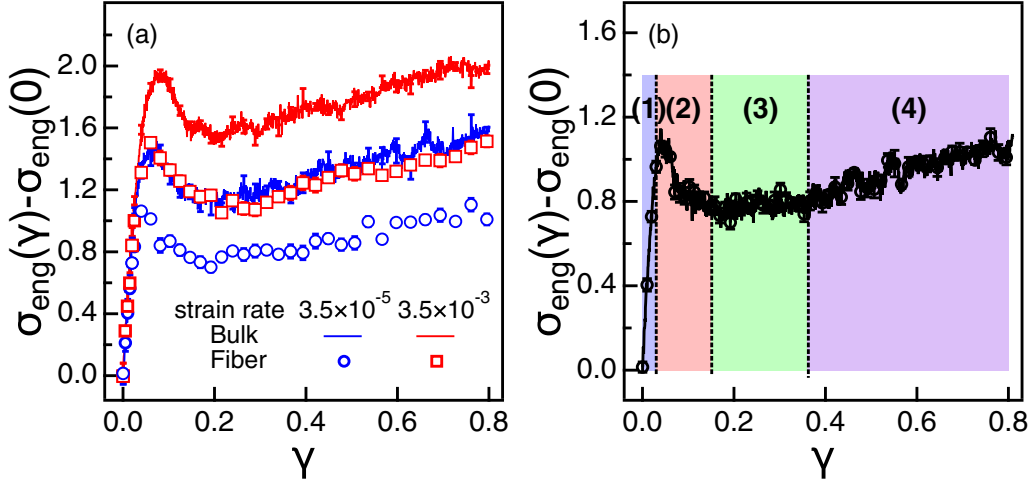


FIG. 3. (a) The stress-strain curves of polymer fiber glasses (empty) and bulk polymer glasses (lines) at $\dot{\gamma} = 3.5 \times 10^{-5} \sigma/\tau$ (blue) and $\dot{\gamma} = 3.5 \times 10^{-3} \sigma/\tau$ (red). These stress-strain curves are obtained at $\Gamma = 1 \times 10^{-5}$. (b) The four regimes of mechanical responses of polymer fiber glasses for $\dot{\gamma} = 3.5 \times 10^{-5} \sigma/\tau$ are indicated: (1) the elastic regime, (2) the stress overshoot regime, (3) the steady-state regime, and (4) the strain hardening regime.

distance between the i th monomer and the central axis. $\langle \dots \rangle$ denotes ensemble averages. We fit simulation results for $\rho(r_r)$ to the following hyperbolic tangent function $\rho(r_r) = \frac{\rho_0}{2} [1 + \tanh(\frac{R_0 - r_r}{l_s})]$. Here ρ_0 is the value of $\rho(r_r)$ at $r_r = 0$. R_0 and l_s denote the estimated radius of the polymer fiber and the width of the interface, respectively. As shown in Fig. 2(b), $\rho(r_r)$ of polymer fibers fits well with the hyperbolic tangent function. Before we begin to deform the fibers, we find that $\rho_0 = 1.04$, $R_0 = 11.68\sigma$, and $l_s = 0.31\sigma$ at $T = 0.1$. One monomer of the coarse-grained bead spring model is usually comparable to the Kuhn monomer of polymers. In the case of polyethylene, the Kuhn length is 1.4 nm. Therefore, the diameter of polymer fibers in our simulations corresponds to about 30 nm, which is a realizable length scale in experiments. For example, Zhou *et al.* reported the nanofibers made of polyaniline, of which the diameter was as low as 20 nm [79].

In order to investigate the mechanical responses of glassy polymer fibers, we undergo the uniaxial deformation of the glassy polymer fibers at $T = 0.1$ along the fiber axis (x axis) at a constant engineering strain rate ($\dot{\gamma}$). We employ the *deform* command incorporated in the LAMMPS simulator. During the uniaxial deformation, the dimension L_x of the simulation cell changes as $L_x(t + \delta t) = L_x(t) + \dot{\gamma} \delta t$, where δt is the elapsed time during the deformation. The x components of the positions of all monomers are remapped to the deformed simulation box. On the other hand, L_y and L_z of simulation cells fluctuate in response to the barostat with $p_y = p_z = 0$ [27]. To obtain stress-strain curves of glassy polymer fibers, we calculate the xx component of engineering strain as $\gamma_{xx} = (L'_x - L_x)/L_x$. We also calculate the xx component of engineering stress (σ_{xx}) of the system as follows:

$$\sigma_{xx} = -\frac{1}{V_0} \left\{ \sum_{i=1}^{N_t} m_i v_{i,x} v_{i,x} + \sum_{i=1}^{N_t-1} \sum_{j=i+1}^{N_t} r_{ij,x} f_{ij,x} \right\}, \quad (4)$$

where i and j denote the particle indices, and V_0 is the volume of the systems before deformation. In the case of polymer fibers, $V_0 = \pi R_0^2 L_x$. $v_{i,x}$ is the x component of the velocity

of the i th particle. $r_{ij,x}$ and $f_{ij,x}$ denote the x components of the distance and the force between the i th and j th particles, respectively. In this study we discuss only the xx components of strain and stress. For convenience' sake, therefore, we drop the subscripts for both the strain (γ) and the stress (σ_{eng}).

We also prepare bulk polymer melts of 250 polymer chains ($N_{\text{pol}} = 250$) with $N_{\text{mon}} = 32$ monomers in order to make a comparison with polymer fibers. We perform NpT molecular dynamics simulations with pressure $p = 0$ and $T = 1$ using the Nosé-Hoover barostat. We equilibrate the bulk polymer melts until the end-to-end vector time correlation function decays to e^{-1} . Then we cool the bulk polymer melts down to $T = 0.1$ at a cooling rate of $\Gamma = 1 \times 10^{-5}$ under NpT condition with $p = 0$. Note that $T = 0.1$ is much lower than T_g of bulk polymer melts. T_g is estimated to be 0.41 as depicted in Fig. 2(a). We also deform the bulk polymer glasses along the x axis at a constant engineering strain rate. The detailed procedure for the uniaxial deformation for the bulk polymer glasses is identical to that for polymer fibers.

III. RESULTS AND DISCUSSIONS

A. The mechanical response of polymer fiber glasses

Both polymer fiber glasses and bulk polymer glasses in our simulations respond to the deformation in a nonlinear fashion. To monitor the mechanical response of polymer fiber glasses, we deform the fibers along the central axis at three strain rates of $\dot{\gamma} = 3.5 \times 10^{-5}$, 3.5×10^{-4} , and $3.5 \times 10^{-3} \sigma/\tau$. During the uniaxial deformation we calculate the engineering stress [$\sigma_{\text{eng}}(\gamma)$] as a function of the engineering strain (γ) for each value of $\dot{\gamma}$ [Fig. 3(a)]. Note that the ordinate in Fig. 3(a) corresponds to the difference in the engineering stress from that for the undeformed state ($\gamma = 0$). Simulation results for the stress-strain curve are categorized clearly into four distinct regimes: (1) the elastic regime, (2) the stress overshoot regime, (3) the steady-state regime, and (4) the strain hardening regime [Fig. 3(b)], which are consistent with previous studies [40,49]. The stress-strain curves of polymeric

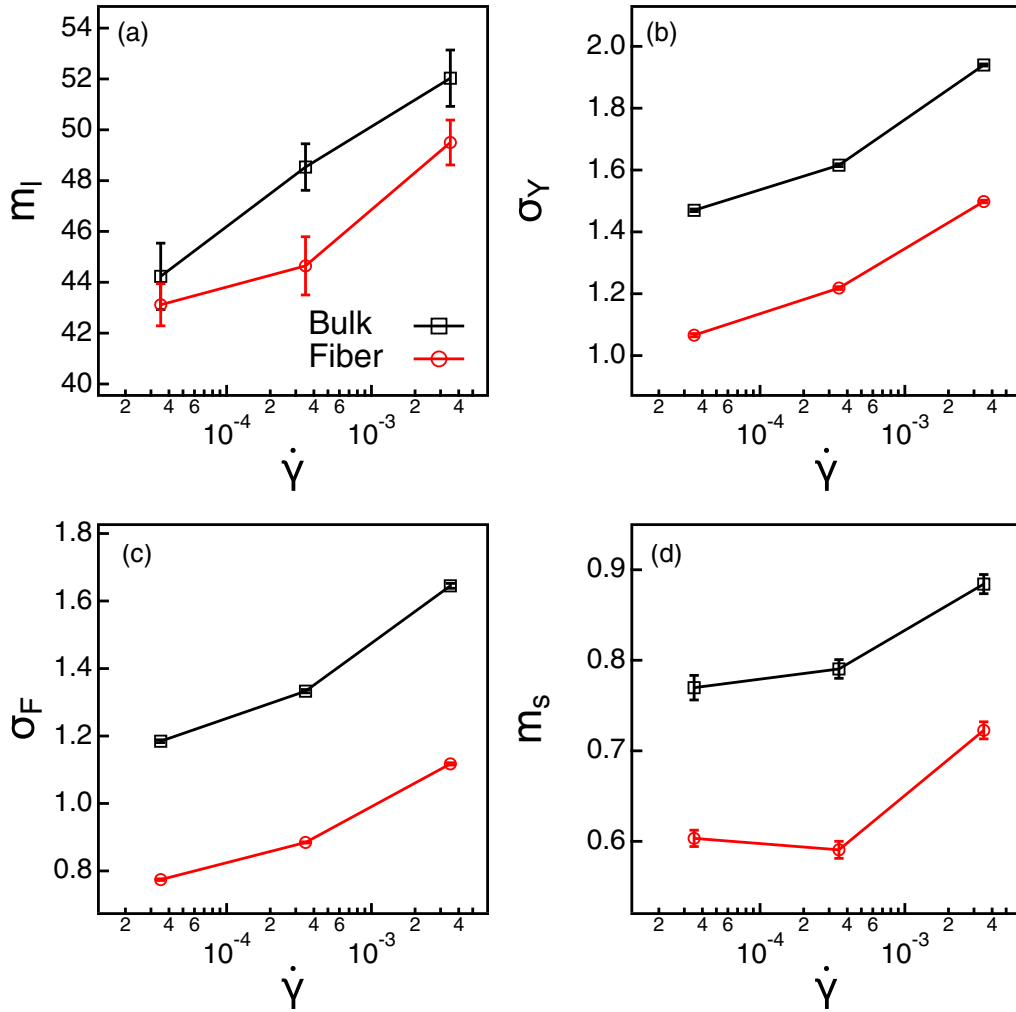


FIG. 4. Simulation results as a function of $\dot{\gamma}$ for (a) the elastic modulus (m_l), (b) the yield stress (σ_Y), (c) the plastic flow stress (σ_F), and (d) strain hardening modulus (m_s) of polymer fiber glasses (red circles) and bulk polymer glasses (black squares). All results are obtained at $\Gamma = 1 \times 10^{-5}$.

systems in our simulations are different from those of monomer glasses and short oligomer glasses qualitatively due to the presence of the strain hardening regime. For example, the stress-strain curves of modified binary Lennard-Jones system for metallic glasses did not exhibit the strain hardening regime at large deformation [80]. The stress-strain curves of polymer glasses and fibers of short oligomers did not exhibit the strain hardening regime at large deformation, either [32,81].

In the elastic regime, $\sigma_{\text{eng}}(\gamma)$ increases linearly with γ . The elastic modulus (m_l) of the regime is determined to be the slope of the stress-strain curve in the elastic regime ($\gamma < 0.005$). In the stress overshoot regime, $\sigma_{\text{eng}}(\gamma)$ reaches a maximum at a yield stress but begins to decrease with a further increase in γ . We determine the yield stress σ_Y to be the value of $\sigma(\gamma) - \sigma(0)$ at the maximum. In the steady-state regime, $\sigma(\gamma) - \sigma(0)$ remains constant over the regime, of which value is taken as the plastic flow stress σ_F . In the last strain hardening regime, $\sigma(\gamma)$ begins to increase again with an increase in γ . The strain hardening modulus (m_s) is, then, the slope of the stress-strain curve in the strain hardening regime. We estimate four mechanical properties (m_l , σ_Y , σ_F , and m_s)

that characterize the mechanical response of glasses upon the deformation (Fig. 4).

All of the mechanical properties are larger for bulk polymer glasses than polymer fiber glasses, and are also dependent on the strain rate ($\dot{\gamma}$). Figure 4 depicts the mechanical properties as functions of $\dot{\gamma}$. m_l , σ_Y , σ_F , and m_s of both glassy polymer fibers and bulk polymer glasses increase with an increase in the strain rate. In the case of bulk polymer glasses, σ_Y and σ_F increase by about 40% from $\dot{\gamma} = 3.5 \times 10^{-5}$ to $\dot{\gamma} = 3.5 \times 10^{-3} \sigma/\tau$. m_l and m_s increase by 15% and 30%, respectively, too. Such a strain-rate dependence of mechanical properties are in agreement with previous experiments and simulation studies. Previous studies on m_l , σ_Y , and σ_F revealed a logarithmic dependence on strain rates [82–84]. Even in the case of the polymer fiber glasses, we find that m_l , σ_Y , and σ_F follow the logarithmic dependence on $\dot{\gamma}$. Previous studies also showed that m_s increases with $\dot{\gamma}$ [82].

As shown in Fig. 3(a), $\sigma_{\text{eng}}(\gamma) - \sigma_{\text{eng}}(0)$ of polymer fiber glasses is lower for a given strain rate ($\dot{\gamma}$) than that of bulk polymer glasses. Note that the value of $\sigma(\gamma = 0)$ of polymer fiber glasses at the undeformed state is 0.66, whereas $\sigma(\gamma = 0) = 0$ for bulk polymer glasses. Such a nonzero stress

at the undeformed state is attributed to the surface tension of the polymer fibers [27]. Note that subtracting the value of the stress at zero strain from the stress-strain curve is not to exclude the contribution of the surface tension to the stress-strain curves of polymer fibers but to compare bulk polymer glasses and polymer fiber glasses. For the comparison of bulk polymer glasses and polymer fiber glasses, it is important to investigate how much the stress increases from the value of the stress of undeformed states, instead of the absolute value of stress. The elastic modulus (m_l) of bulk polymer glasses is larger than that of polymer glass fibers by about 2% at $\dot{\gamma} = 3.5 \times 10^{-5} \sigma / \tau$, which is consistent with previous simulation studies [27,40,43]. For example, Buell *et al.* [27] showed that m_l decreased with a decrease in the fiber radius. We also find that σ_y , σ_F , and m_s of polymer fiber glasses are lower than those of bulk polymer glasses [Figs. 4(b)–4(d)], which shall be discussed in the following sections.

In this study we perform simulations under the condition that the morphology of fibers is stable during deformation. Although we find the surface distortion of polymer fibers in some trajectories at a large strain, as shown in Fig. 3(a), the stress-strain curves of polymer fibers do not exhibit a decrease in engineering stress due to the necking [85]. Also note that we consider the stability of the fiber morphology based on the Rayleigh instability criterion [86]. According to the Rayleigh instability criterion, if $2\pi R_0 \ll L_x$, fibers are unstable. Before deformation, the radius of fibers is 11.68σ and the length of our system along the fiber axis is 25σ . Therefore, $2\pi R_0/L_x = 11.68\sigma \times 2\pi/25\sigma \gg 1$, which suggests that fibers before deformation should be stable. But, at a large strain of 0.8, the radius of fibers is 8.64σ and the length of the system along the fiber axis becomes 45.42σ . Then $2\pi R_0/L_x = 8.64\sigma \times 2\pi/45.417\sigma \approx 1.2$ such that the fiber is still relatively stable than other polymer nanofibers in experiments.

We also obtain the stress-strain curves of polymer fibers of much longer chains with $N_{\text{mon}} = 200$. Polymer chains of $N_{\text{mon}} = 200$ are usually entangled in polymer melts [87]. As shown in Fig. 5, before the strain hardening regime, both stress-stress curves are almost the same. However, the strain hardening modulus of polymer fibers of long chains (0.760) is larger than that of polymer fibers of short chains (0.603). These results for the effects of the chain length are consistent with previous simulation results and experimental results. For example, previous experiments for a thermoplastic glassy polyimide showed that the values of the Young's modulus were constant regardless of molecular weights of polyimide at room temperature [88]. Previous simulation results also showed that the strain hardening modulus increased with the chain length [32].

B. Local mechanical properties

We scrutinize the local responses of the polymer fiber glasses and their spatial heterogeneity in mechanical properties. This allows us to elucidate the effects of the surface and the confinement on the mechanical response. We calculate the local elastic modulus of surface layers of polymer fibers. We divide the cross section of polymer fibers into each layer along the radial direction like Fig. 6(a). The thickness of each

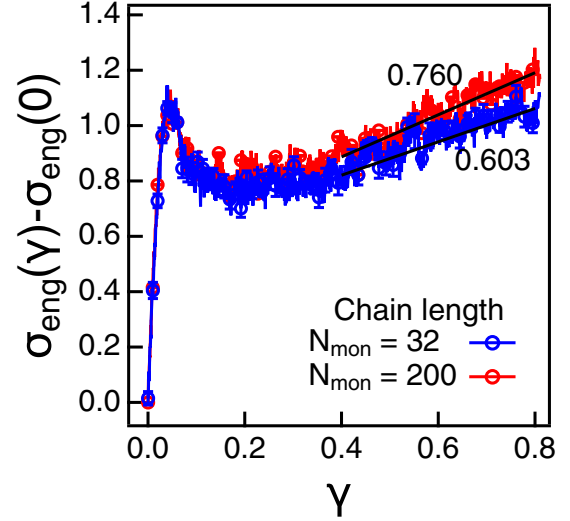


FIG. 5. The stress-strain curves of polymer fiber glasses of short chains of 32 monomers (blue) and long chains of 200 monomers (red). The strain rate is $3.5 \times 10^{-5} \sigma / \tau$ and the cooling rate is 1×10^{-5} .

layer is 0.5σ . Then we obtain the local stress-strain curves of polymer fibers and estimate local elastic modulus of each layer from the local stress-strain curves. The local stress is estimated [89] as follows:

$$\sigma^\alpha = -\frac{1}{V^\alpha} \left[\sum_{i=1}^{N_i^\alpha} m_i v_{i,x} v_{i,x} + \sum_{i=1}^{N_i^\alpha-1} \sum_{j=i+1}^{N_i^\alpha} r_{ij,x} f_{ij,x} \frac{q_{ij}^\alpha}{r_{ij}} \right], \quad (5)$$

where α is the index for each layer of polymer fibers. N_i^α and V^α denote the number of monomers and the volume of the corresponding layer during the deformation, respectively. r_{ij} is the distance between the i th and the j th particles. q_{ij}^α is the part of the line segment connecting between the i th particle and the j th particle that lies inside the α layer. If the line segment connecting between the i th particles and j th particles lies inside only α layer, $q_{ij}^\alpha = 1$ and the contribution of the

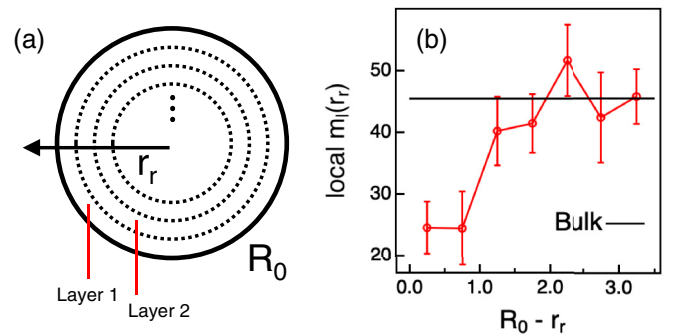


FIG. 6. (a) A schematic figure of layers of polymer fibers. R_0 is the radius of polymer fibers and r_r is the shortest distance from the central axis of the fiber. $R_0 - r_r = 0$ means the surface of polymer fibers. The thickness of layers is 0.5σ . (b) The local elastic modulus of polymer fibers as a function of r_r . A black line is the elastic modulus of bulk polymer glasses. The strain rate is $3.5 \times 10^{-5} \sigma / \tau$ and the cooling rate is 1×10^{-5} .

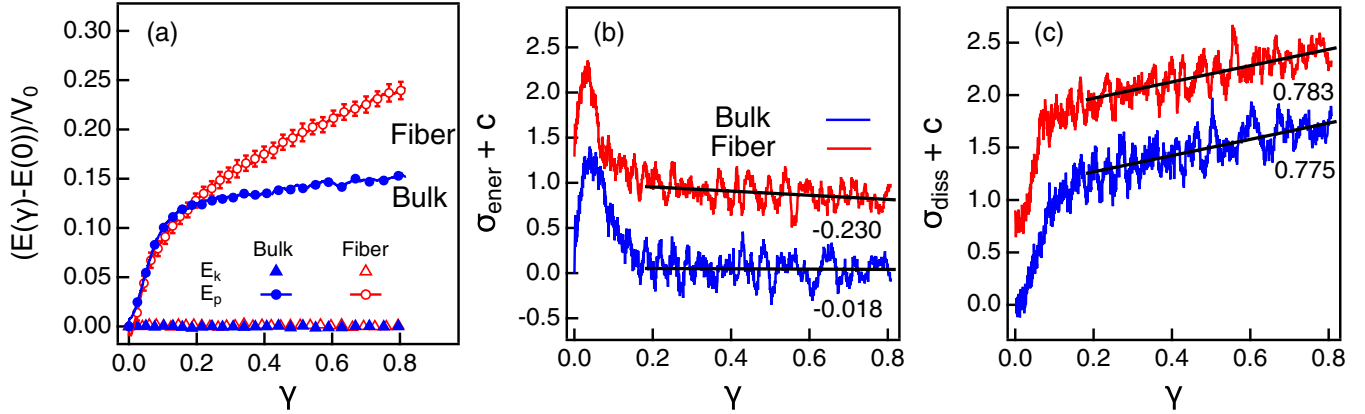


FIG. 7. (a) The difference in the kinetic energy density (E_k/V_0) and the potential energy density (E_p/V_0) between the undeformed system and the deformed system at $\dot{\gamma} = 3.5 \times 10^{-5} \sigma/\tau$ and $\Gamma = 1 \times 10^{-5}$. (b) The energetic stress (σ_{ener}) of the polymer fiber glasses (red) and the bulk polymer glasses (blue). (c) The dissipative stress (σ_{diss}) of the polymer fiber glasses (red) and the bulk polymer glasses (blue) at $\dot{\gamma} = 3.5 \times 10^{-5} \sigma/\tau$. All curves in (b) and (c) are shifted by the constant C for the sake of clarity.

interaction between the i th particle and j th particle to the local stress of other layers is zero.

Figure 6(b) depicts the local modulus of polymer fibers as a function of $R_0 - r_r$. Here r_r is the shortest distance between the monomer and the central fiber axis, and R_0 is the diameter of the polymer fiber. Therefore $R_0 - r_r \approx 0$ corresponds to the surface region of the fiber. The local elastic modulus (local $m_l \approx 25$) of the surface region is about 1.8 times smaller than local modulus (local $m_l \approx 45$) of the core region, while the local m_l of the core region is quite close to that of the bulk polymer glasses (Fig. 6). This indicates that monomers experience quite heterogeneous mechanical responses under deformation depending on the region that the monomers belong to. And the mechanical environment of the core region is similar to that of the bulk polymer glasses. This is consistent with previous experiments on the local modulus of MEH-PPV fibers where the local modulus of the core region is about two times larger than that of the surface region [44].

The local modulus of polymer fiber glasses [Fig. 6(b)] suggests that the thickness of the surface region would be about 1σ . The thickness of surface region in our work is comparable to the previous results of polyethylene atomic simulations (1–3 nm) [27] and also measurable in experiments. (In the case of polyethylene, for example, 1σ is comparable to 1.4 nm.) One caveat is that 1σ is the shortest length scale in our coarse-grained model. In order to investigate the size of the surface layer at a higher resolution, one might have to employ a finer model with atomistic details for monomers. On the other hand, note also that in order to define the surface layer, we estimate the local modulus, i.e., how much force monomers within a certain layer experience as the monomers are displaced during the deformation. And the displacement of monomers of 1σ is not small in polymer glasses, considering that the maximum nonaffine displacement of polymer fiber glasses is about only 0.37σ (as shall be discussed later). Within the surface layer of 1σ , therefore, highly nonaffine monomers can be distributed continuously.

Composite material theory provided an approach to explain the elastic modulus of the polymer fibers. The composite material theory assumes that the elastic modulus of the core region would be identical to the bulk polymer glasses and also

that the surface region would be more soft with a smaller elastic modulus. Then, the theory suggests that the elastic modulus of the polymer fibers would be a linear combination, i.e., $m_l \approx m_l^{\text{core}} f_{\text{core}} + m_l^{\text{surf}} f_{\text{surf}}$. Here f_{core} is the volume fraction of the core region and $f_{\text{surf}} = 1 - f_{\text{core}}$. m_l obtained from the theory matches well with the value of m_l from our simulations, which corroborates the composite material theory.

C. Energetic and dissipative stresses

For both polymer fiber glasses and the bulk polymer glasses, the nonbonding interactions between monomers are mainly responsible for the mechanical response to the deformation. Figure 7(a) depicts differences in either the kinetic energy density (E_k/V_0) or the potential energy density (E_p/V_0) between the undeformed ($\gamma = 0$) and the deformed state as a function of γ with $\dot{\gamma} = 3.5 \times 10^{-5} \sigma/\tau$. E_k stays constant during the uniaxial deformation because we perform canonical isothermal simulations at each value of γ . On the other hand, not surprisingly, the potential energies (E_p) of both polymer fiber glasses (red) and bulk polymer glasses (blue) increase upon the deformation. At a relatively large strain beyond the yield point, E_p/V_0 of the fiber glasses increases more quickly than that of the bulk polymer glasses. We dissect the potential energy E_p into the bonding potential (U_b) and the nonbonding potential (U_{nb}) contributions. We find that the increase in the E_p upon the deformation is attributed mainly to the nonbonding interactions between monomers. U_b hardly changes but only fluctuates during the deformation. This indicates that the bond relaxation (which is the shortest relaxation mode in the polymer chain) occurs quickly during the deformation. On the other hand, U_{nb} increases upon the deformation.

We decompose the stress of the polymer fiber glasses into (1) an energetic (σ_{ener}) and (2) a dissipative (σ_{diss}) stresses based on the first law of thermodynamics ($dE = dW + dQ$) as follows:

$$\sigma_{\text{eng}} = \frac{\partial W}{\partial \gamma} = \frac{\partial E}{\partial \gamma} + \frac{\partial(-Q)}{\partial \gamma} = \sigma_{\text{ener}} + \sigma_{\text{diss}}, \quad (6)$$

where W , E , and $-Q$ denote the work done on the system per volume, the internal energy of the system per volume, and the

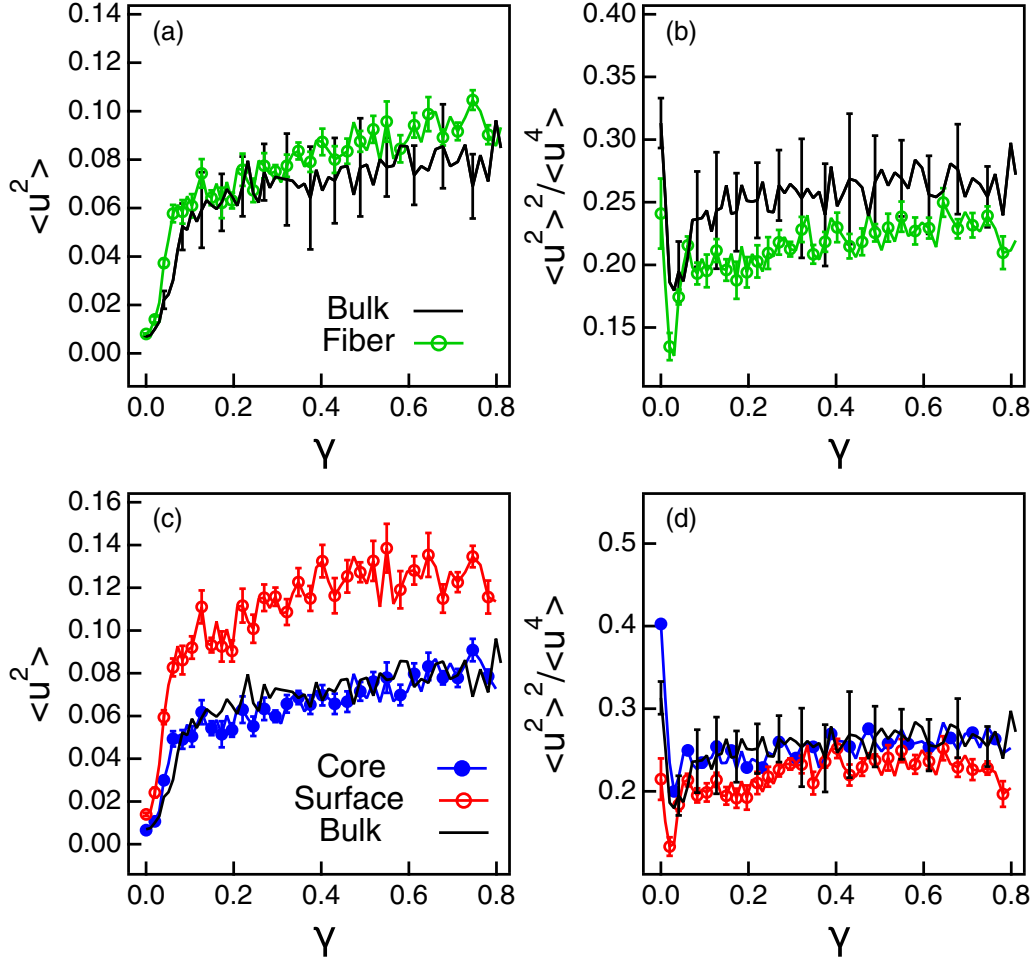


FIG. 8. (a) The mean square nonaffine displacement ($\langle u^2 \rangle$) of bulk polymer glasses (black) and the polymer fiber glasses (green). (b) The participation ratio ($\langle u^2 \rangle^2 / \langle u^4 \rangle$) of the nonaffine displacement of the bulk polymer melts (black) and polymer fiber glasses (green). (c) $\langle u^2 \rangle$ of monomers in the core (blue) and the surface (red) regions of the polymer fiber glasses. A black line corresponds to the $\langle u^2 \rangle$ of the bulk polymer glasses. (d) $\langle u^2 \rangle^2 / \langle u^4 \rangle$ of monomers in the core (blue) and the surface (red) regions of the polymer fiber glasses. A black line corresponds to the $\langle u^2 \rangle^2 / \langle u^4 \rangle$ of the bulk polymer glasses. In this figure, $\dot{\gamma} = 3.5 \times 10^{-5} \sigma / \tau$ and $\Gamma = 1 \times 10^{-5}$.

heat transfer *away* from the system per volume, respectively. We estimate σ_{ener} by calculating the derivative of E_p with respect to γ because E_k stays constant. Then σ_{diss} can be obtained by using $\sigma_{\text{diss}} = \sigma_{\text{eng}} - \sigma_{\text{ener}}$.

The energetic stress (σ_{ener}) and the dissipative stress (σ_{diss}) contribute differently to the total stress depending on the regimes [Figs. 7(b) and 7(c)]. σ_{ener} increases sharply initially with γ and contributes significantly to the elastic regime. However, σ_{ener} decreases back in the steady-state and the strain hardening regimes while σ_{diss} should account for the increase in the stress in the strain hardening regime. As depicted in Fig. 7(c), σ_{diss} keeps increasing beyond the yield point with a slope of about 0.78 for both polymer fiber glasses and bulk polymer glasses. On the other hand, σ_{ener} decreases in the post-yield regime with a negative slope. The slope of the σ_{ener} of the polymer fiber glasses is even lower around -0.23 than that (-0.02) of the bulk polymer glasses. This is why the strain-hardening modulus (m_s) is lower for the polymer fiber glasses. The dominant contribution of σ_{diss} in the strain hardening regime are consistent with previous studies [74,75]. We discuss the nonaffine displacement distribution of monomers

in the following section, which relates to the dramatic increase in σ_{diss} beyond the yield point.

D. Nonaffine displacement during deformation

We investigate the plastic flow of glasses beyond the yield points by calculating the mean square nonaffine displacement ($\langle u^2 \rangle$) and the participation ratio ($\langle u^2 \rangle^2 / \langle u^4 \rangle$) of the nonaffine displacement. In the affine deformation, particles during deformation are placed on the position expected by the global strain (γ) applied to the system. In general, crystalline solids are expected to be affinely deformed. Beyond the yield points, however, the plastic flow could locate particles away from the positions expected by the global strain, thus resulting in the nonaffine deformation. We capture nonaffine deformation of glasses by calculating the mean square nonaffine displacement ($\langle u^2 \rangle$). In order to obtain both $\langle u^2 \rangle$ and $\langle u^2 \rangle^2 / \langle u^4 \rangle$ as functions of the strain (γ), we take four steps as follows. Note that the symbol “o” indicates the simulation parameters and configurations used (and obtained) from the additional simulations for the estimation of the nonaffine displacement. (Step 1) We

take a simulation configuration at a given strain value of γ and determine the position vector (\vec{r}_{iy}°) of the i th monomer. (Step 2) We, then, undergo the uniaxial and affine deformation with a strain of $\gamma_{xx}^\circ = 0.005$ and $\gamma_{yy}^\circ = \gamma_{zz}^\circ = \frac{1}{\sqrt{1+\gamma_{xx}^\circ}} - 1$. Here γ_{xx}° , γ_{yy}° , and γ_{zz}° denote the strains in x , y , and z directions, respectively. This affine deformation allows us to determine the position vector (\vec{r}_{ia}°) of the i th monomer if the monomer were to undergo the affine displacement. (Step 3) Then we perform additional canonical NVT simulations with a configuration (\vec{r}_{ia}°) at a strain of γ (in step 2) at $T = 0.1$ during $t = 20000\tau$. In this step, monomers may relax its configurations toward the local free energy minima at the given γ and undergo the nonaffine movements. (Step 4) The position vector (\vec{r}_i°) of the i th monomer obtained in the previous step is determined to be the nonaffine position vector. Then the nonaffine displacement vector (\vec{u}) is defined as $\vec{u} \equiv \vec{r}_i^\circ - \vec{r}_{ia}^\circ$.

As expected, the deformation of both fibers and bulk polymer glasses is affine in the elastic regime with $\langle u^2 \rangle \approx 0$ [Fig. 8(a)]. However, after the elastic regime, $\langle u^2 \rangle$ increases rapidly, thus indicating that monomers begin to undergo nonaffine displacement significantly. Beyond $\gamma = 0.35$, in the case of polymer fibers, the magnitude of $\langle u^2 \rangle$ increases gradually. On the other hand, in the case of bulk polymer glasses, the magnitude of $\langle u^2 \rangle$ converges to a constant value.

The participation ratio ($\langle u^2 \rangle^2 / \langle u^4 \rangle$) is a measure of how much nonaffine displacement deviates from the Gaussian statistics [31]. If the nonaffine displacement distribution of monomers is Gaussian, $\langle u^2 \rangle^2 / \langle u^4 \rangle = 3/5$. A smaller value of $\langle u^2 \rangle^2 / \langle u^4 \rangle$ suggests that nonaffine displacement deviates from Gaussian statistics and that monomers would undergo more correlated motions. As shown in Fig. 8(b), $\langle u^2 \rangle^2 / \langle u^4 \rangle$ decreases in the elastic regime, thus indicating that monomers are likely to participate in the correlated motions in the elastic regime. After yield point, however, $\langle u^2 \rangle^2 / \langle u^4 \rangle$ increases, and then converges in the steady-state regime and the strain hardening regime. This shows that the nonaffine displacements of monomers becomes relatively homogeneous compared to those in the elastic regime, which is consistent with previous studies [31,66].

The deformation of polymer fiber glasses is more nonaffine, especially in the interfacial regions, than that of bulk polymer glasses. As shown in Fig. 8(a), $\langle u^2 \rangle$ is larger for polymer fiber glasses than for bulk polymer glasses. In the case of polymer fiber glasses, we divide $\langle u^2 \rangle$ into two contributions from the surface and core regions, i.e., $\langle u^2 \rangle_{\text{surf}}$ and $\langle u^2 \rangle_{\text{core}}$. As shown in Fig. 6(b), the local elastic modulus increases rapidly after $r_r < R_0 - 1\sigma$, for which we set the thickness of surface region as 1σ . If a monomer is located close to the fiber axis with $r_r < R_0 - 1\sigma$, the monomer belongs to the core region. Monomers that lie outside the core region with $r_r > R_0 - 1\sigma$ are considered to be in the surface region. Interestingly, $\langle u^2 \rangle_{\text{core}}$ of the core region is almost identical to that in the bulk polymer glasses [Fig. 8(c)], while $\langle u^2 \rangle_{\text{surf}}$ in the surface region is much larger than $\langle u^2 \rangle_{\text{core}}$. The significant nonaffine displacement in the surface region should be responsible for the more nonaffine deformation of the polymer fiber glasses. We also find that $(\langle u^2 \rangle^2 / \langle u^4 \rangle)_{\text{surf}}$ in the surface region is lower than $(\langle u^2 \rangle^2 / \langle u^4 \rangle)_{\text{core}}$ in the core region, and that $(\langle u^2 \rangle^2 / \langle u^4 \rangle)_{\text{core}}$ collapses well onto $\langle u^2 \rangle^2 / \langle u^4 \rangle$ of bulk

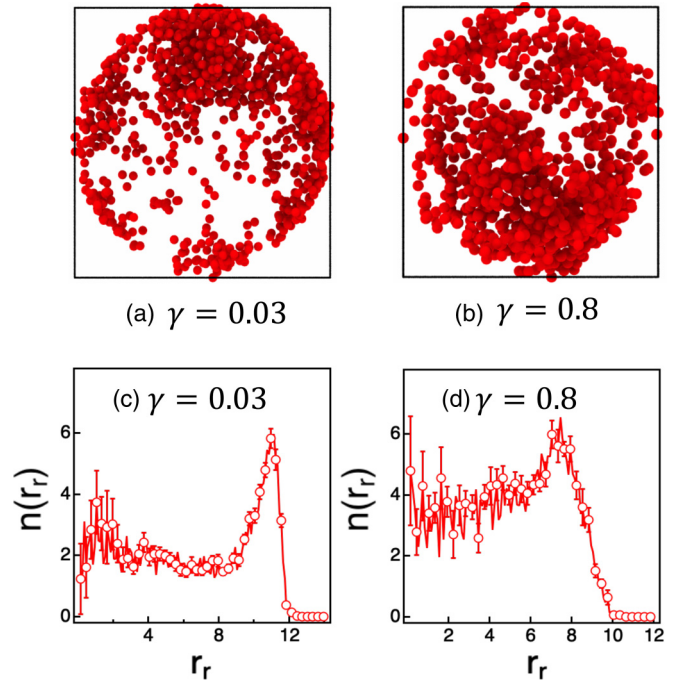


FIG. 9. The highly nonaffine monomers projected on the cross section of the fiber at (a) $\gamma = 0.03$ and (b) $\gamma = 0.8$. The number distribution functions [$n(r_r)$] of monomers with top 10% of the magnitude of nonaffine displacements as a function of r_r at (c) $\gamma = 0.03$ and (d) $\gamma = 0.8$. In this figure, $\dot{\gamma} = 3.5 \times 10^{-5} \sigma / \tau$ and $\Gamma = 1 \times 10^{-5}$.

polymer glasses after the elastic regime. This suggests that the nonaffine displacements of monomers in the surface region are more correlated than the bulk polymer glasses and the core region of the fibers.

We project highly nonaffine monomers onto the cross section of the polymer fiber glass. We determine that monomers with top 10% of the magnitude of nonaffine displacements are *highly nonaffine* monomers. As depicted in Fig. 9, such highly nonaffine monomers are distributed mainly in the surface region at $\gamma = 0.03$. As shown in Fig. 9(c), the number of highly nonaffine monomers in the surface region is three times larger than that in the core region. At $\gamma = 0.8$, however, monomers at the core region are also likely to perform nonaffine displacement. As shown in Fig. 9(d), the number of highly nonaffine monomers in the surface region is only 1.5 times larger than that in the core region. This indicates that at a small strain, the nonaffine displacement of monomers are spatially heterogeneous with the most highly nonaffine monomers in the surface region. However, at a large strain regime, the nonaffine displacement distribution becomes relatively widespread, which is consistent with our result that $\langle u^2 \rangle^2 / \langle u^4 \rangle$ increases with γ .

The nonaffine displacement ($\langle u^2 \rangle$) also depends on the strain rate ($\dot{\gamma}$). Beyond the elastic regime, especially, $\langle u^2 \rangle$ is larger for a faster strain rate ($\dot{\gamma}$). For example, at $\gamma = 0.6$, $\langle u^2 \rangle$ of the polymer fiber glasses at $\dot{\gamma} = 3.5 \times 10^{-3} \sigma / \tau$ is 2.5 times larger than that at $\dot{\gamma} = 3.5 \times 10^{-5} \sigma / \tau$. The participation ratio of $\langle u^2 \rangle^2 / \langle u^4 \rangle$ at the fast strain rate is also greater than at the slow strain rate. Such dependence of nonaffine displacement on strain rates contributes to the increase of σ_{diss}

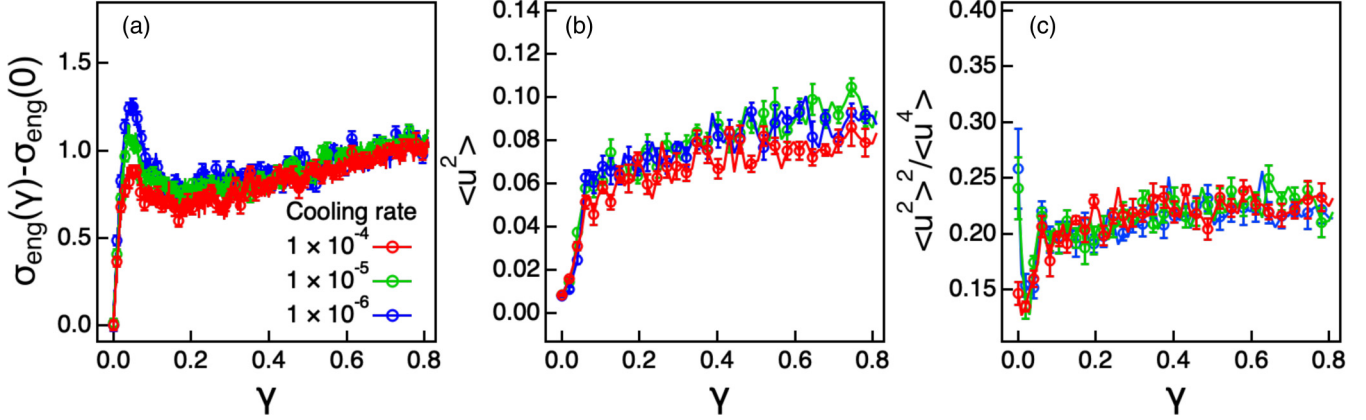


FIG. 10. (a) The stress-strain curves of polymer fiber glasses at $\dot{\gamma} = 3.5 \times 10^{-5} \sigma/\tau$. (b) The mean square nonaffine displacement ($\langle u^2 \rangle$) of polymer fiber glasses. (c) The participation ratio ($\langle u^2 \rangle / \langle u^4 \rangle$) of the nonaffine displacement of polymer fiber glasses. Red markers, green markers, and blue markers represent a cooling rate = $1 \times 10^{-4} \sigma/\tau$, $1 \times 10^{-5} \sigma/\tau$, and $1 \times 10^{-6} \sigma/\tau$, respectively.

after the elastic regime in Fig. 7(c), because the nonaffine displacement relates closely to irreversible rearrangement of monomer under deformation.

We also investigate the effects of the cooling rate on the mechanical properties of polymer fibers. As shown in Fig. 10(a), the values of the yield stress increase with a decrease in cooling rates. These results are consistent with the previous simulation results [49]. Unlike the stress-strain curves, however, the cooling rates do not affect the mean square nonaffine displacement and the participation ratio of the nonaffine displacement in our simulations [Figs. 10(b) and 10(c)]. These results imply that the nonaffine displacement defined in our work should not be sensitive to the cooling rates. According to the previous simulation work [49], the nonaffine behavior defined at long timescale could be affected by the cooling rate. But, the nonaffine displacement in our study is defined at a short timescale.

IV. SUMMARY AND CONCLUSION

We perform molecular dynamic simulations to investigate the mechanical response of polymer fiber glasses. We deform the polymer fibers in a uniaxial fashion along the fiber axis and obtain the stress-strain curves for different strain rates. Stress-strain curves obtained from our simulations are categorized clearly into four regimes as in the experiments: (1) the elastic regime, (2) the stress overshoot regime, (3) the steady-state regime, and (4) the strain hardening regime. We estimate the mechanical properties (the elastic modulus, the yield stress, the steady-state stress, and the strain hardening modulus) that characterize the stress-strain curve. They all increase with an increase in the strain rate and differ from those of bulk polymer glasses.

The difference in the mechanical properties between polymer fiber glasses and bulk polymer glasses is attributed to the fact that the mechanical response of polymer fiber glasses is spatially heterogeneous. We calculate the local modulus of polymer fibers for both core and surface regions. The elastic modulus of the core region is similar to that of bulk polymer glasses while the elastic modulus becomes lower in the surface region.

The difference in the strain hardening modulus between the polymer fiber glasses and the bulk polymer glasses may be explained by observing the energetic and dissipative contributions to the stress. We find that the energetic stress contributes mainly to the mechanical properties in the pre-yield regime while the dissipative stress becomes dominant in the post-yield regime. The slope of the dissipative stress of polymer fiber glasses in the strain hardening regime is similar to that of bulk polymer glasses. However, the slope of energetic stress of fibers in the strain hardening regime is negative unlike the slope of energetic stress of bulk polymer glasses (which is close to zero). Such a negative slope of the energetic stress leads to a smaller strain hardening modulus for the polymer fiber glasses.

We also estimate the nonaffine displacement of polymers during glassy polymer fibers. We find that highly nonaffine particles are located mainly at the surface region and also that the nonaffine displacement at the surface region shows the correlated motion in the pre-yield. But, in the post-yield regime, highly nonaffine particles are widespread throughout the fibers.

ACKNOWLEDGMENTS

The authors would like to thank Professor Riggelman for valuable comments and advice regarding the simulations. This research was supported by the Basic Science Research Program through the National Research Foundation of Korea (NRF) funded by the Ministry of Education (2018R1A6A1A03024940). This research was also supported by the Creative Materials Discovery Program (2018M3D1A1057844) through the NRF funded by the Ministry of Science and ICT. This work was supported by the National Research Foundation of Korea (NRF) grant funded by the Korea government (MSIT) (2019R1A2C2084053). This work was supported by Korea Environment Industry & Technology Institute (KEITI) through Technology Development Project for Safety Management of Household Chemical Products Program, funded by Korea Ministry of Environment (MOE) (Grant No. 2020002960002).

- [1] J. A. Forrest, K. Dalnoki-Veress, J. R. Stevens, and J. R. Dutcher, *Phys. Rev. Lett.* **77**, 2002 (1996).
- [2] J. L. Keddie, R. A. L. Jones, and R. A. Cory, *Europhys. Lett.* **27**, 59 (1994).
- [3] G. B. DeMaggio, W. E. Frieze, D. W. Gidley, M. Zhu, H. A. Hristov, and A. F. Yee, *Phys. Rev. Lett.* **78**, 1524 (1997).
- [4] M. Alcoutlabi and G. B. McKenna, *J. Phys.: Condens. Matter* **17**, R461 (2005).
- [5] M. D. Ediger and J. A. Forrest, *Macromolecules* **47**, 471 (2014).
- [6] Y. Li and W. Wan, *IEEE Nanotechnol. Mag.* **11**, 16 (2017).
- [7] Y. H. Liu, D. Wang, K. Nakajima, W. Zhang, A. Hirata, T. Nishi, A. Inoue, and M. W. Chen, *Phys. Rev. Lett.* **106**, 125504 (2011).
- [8] N. Wang, J. Ding, F. Yan, M. Asta, R. O. Ritchie, and L. Li, *Npj Comput. Mater.* **4**, 19 (2018).
- [9] B. Shang, J. Rottler, P. Guan, and J.-L. Barrat, *Phys. Rev. Lett.* **122**, 105501 (2019).
- [10] W. He, T. Yong, W. E. Teo, Z. Ma, and S. Ramakrishna, *Tissue Eng.* **11**, 1574 (2005).
- [11] J. Venugopal and S. Ramakrishna, *Appl. Biochem. Biotechnol.* **125**, 147 (2005).
- [12] D. R. Nisbet, J. S. Forsythe, W. Shen, D. I. Finkelstein, and M. K. Horne, *J. Biomater. Appl.* **24**, 7 (2009).
- [13] Y. Zhang, C. T. Lim, S. Ramakrishna, and Z.-M. Huang, *J. Mater. Sci.: Mater. Med.* **16**, 933 (2005).
- [14] H. S. Yoo, T. G. Kim, and T. G. Park, *Adv. Drug Delivery Rev.* **61**, 1033 (2009).
- [15] X. Hu, S. Liu, G. Zhou, Y. Huang, Z. Xie, and X. Jing, *J. Control. Release* **185**, 12 (2014).
- [16] I. S. Chronakis, *J. Mater. Process Tech.* **167**, 283 (2005).
- [17] L. Y. Yeo and J. R. Friend, *J. Exp. Nanosci.* **1**, 177 (2006).
- [18] H. W. Cho, S. W. Kim, J. Kim, U. J. Kim, K. Im, J.-J. Park, and B. J. Sung, *J. Chem. Phys.* **144**, 194903 (2016).
- [19] L. Ji, Z. Lin, A. J. Medford, and X. Zhang, *Carbon* **47**, 3346 (2009).
- [20] M. J. Laudenslager, R. H. Scheffler, and W. M. Sigmund, *Pure Appl. Chem.* **82**, 2137 (2010).
- [21] J. Li, Z. Sun, and F. Yan, *Adv. Mater.* **24**, 88 (2012).
- [22] K. Nayak, D. J. Read, T. C. B. McLeish, P. J. Hine, and M. Tassieri, *J. Polym. Sci. B Polym. Phys.* **49**, 920 (2011).
- [23] A. Arinstein and E. Zussman, *J. Polym. Sci. B Polym. Phys.* **49**, 691 (2011).
- [24] A. Arinstein, M. Burman, O. Gendelman, and E. Zussman, *Nat. Nanotechnol.* **2**, 59 (2007).
- [25] A. Milani, M. Casalegno, C. Castiglioni, and G. Raos, *Macromol. Theory Simul.* **20**, 305 (2011).
- [26] J. M. Torres, C. Wang, E. B. Coughlin, J. P. Bishop, R. A. Register, R. A. Riggleman, C. M. Stafford, and B. D. Vogt, *Macromolecules* **44**, 9040 (2011).
- [27] S. Buell, K. J. Van Vliet, and G. C. Rutledge, *Macromolecules* **42**, 4887 (2009).
- [28] R. Rzehak and W. Zimmermann, *Phys. Rev. E* **68**, 021804 (2003).
- [29] N. V. Priezjev, *Phys. Rev. E* **89**, 012601 (2014).
- [30] S. M. Soik and T. A. Sharp, *Phys. Rev. E* **99**, 052505 (2019).
- [31] R. A. Riggleman, H.-N. Lee, M. D. Ediger, and J. J. de Pablo, *Soft Matter* **6**, 287 (2010).
- [32] R. S. Hoy and M. O. Robbins, *Phys. Rev. E* **77**, 031801 (2008).
- [33] M. Wendlandt, T. A. Tervoort, and U. W. Suter, *J. Polym. Sci. B Polym. Phys.* **48**, 1464 (2010).
- [34] K. Paeng, S. F. Swallen, and M. D. Ediger, *J. Am. Chem. Soc.* **133**, 8444 (2011).
- [35] R. J. Masurel, P. Gelineau, S. Cantournet, A. Dequidt, D. R. Long, F. Lequeux, and H. Montes, *Phys. Rev. Lett.* **118**, 047801 (2017).
- [36] O. K. C. Tsui, T. P. Russell, and C. J. Hawker, *Macromolecules* **34**, 5535 (2001).
- [37] S. Curgul, K. J. Van Vliet, and G. C. Rutledge, *Macromolecules* **40**, 8483 (2007).
- [38] K. Paeng, R. Richert, and M. D. Ediger, *Soft Matter* **8**, 819 (2012).
- [39] H. W. Cho and B. J. Sung, *Soft Matter* **13**, 1190 (2017).
- [40] S. Tang, Y. Li, W. K. Liu, and X. X. Huang, *Macromolecules* **47**, 6503 (2014).
- [41] W. Xia and S. Keten, *J. Mater. Res.* **30**, 36 (2015).
- [42] A. D. S. Parmar, S. Kumar, and S. Sastry, *Phys. Rev. X* **9**, 021018 (2019).
- [43] R. J. S. Ivancic and R. A. Riggleman, *Soft Matter* **15**, 4548 (2019).
- [44] A. Camposeo, I. Greenfeld, F. Tantussi, S. Pagliara, M. Moffa, F. Fuso, M. Allegrini, E. Zussman, and D. Pisignano, *Nano Lett.* **13**, 5056 (2013).
- [45] M. Naraghi, I. Chasiotis, H. Kahn, Y. Wen, and Y. Dzenis, *Rev. Sci. Instrum.* **78**, 085108 (2007).
- [46] D. Hossain, M. A. Tschopp, D. K. Ward, J. L. Bouvard, P. Wang, and M. F. Horstemeyer, *Polymer* **51**, 6071 (2010).
- [47] D. Hudzinsky, M. A. J. Michels, and A. V. Lyulin, *J. Chem. Phys.* **137**, 124902 (2012).
- [48] S. Cheng and S.-Q. Wang, *Phys. Rev. Lett.* **110**, 065506 (2013).
- [49] A. Shavit and R. A. Riggleman, *Phys. Chem. Chem. Phys.* **16**, 10301 (2014).
- [50] P. K. Jaiswal, I. Procaccia, C. Rainone, and M. Singh, *Phys. Rev. Lett.* **116**, 085501 (2016).
- [51] C. Chui and M. C. Boyce, *Macromolecules* **32**, 3795 (1999).
- [52] F. M. Capaldi, M. C. Boyce, and G. C. Rutledge, *Phys. Rev. Lett.* **89**, 175505 (2002).
- [53] F. M. Capaldi, M. C. Boyce, and G. C. Rutledge, *Polymer* **45**, 1391 (2004).
- [54] J. Li, T. Mulder, B. Vorselaars, A. V. Lyulin, and M. A. J. Michels, *Macromolecules* **39**, 7774 (2006).
- [55] B. Vorselaars, A. V. Lyulin, and M. A. J. Michels, *J. Chem. Phys.* **130**, 074905 (2009).
- [56] M. Warren and J. Rottler, *Phys. Rev. Lett.* **104**, 205501 (2010).
- [57] B. D. Vogt, *J. Polym. Sci. B Polym. Phys.* **56**, 9 (2018).
- [58] J. Ricci, T. Bennin, and M. D. Ediger, *Macromolecules* **51**, 7785 (2018).
- [59] B. Bending, K. Christison, J. Ricci, and M. D. Ediger, *Macromolecules* **47**, 800 (2014).
- [60] Y. Chen, S. A. Rogers, S. Narayanan, J. L. Harden, and R. L. Leheny, *Phys. Rev. Mater.* **4**, 035602 (2020).
- [61] H.-N. Lee, R. A. Riggleman, J. J. de Pablo, and M. D. Ediger, *Macromolecules* **42**, 4328 (2009).
- [62] H. Mizuno and R. Yamamoto, *J. Chem. Phys.* **136**, 084505 (2012).
- [63] M. Hassani, A. E. Lagogianni, and F. Varnik, *Phys. Rev. Lett.* **123**, 195502 (2019).
- [64] T. Hoshino, S. Fujinami, T. Nakatani, and Y. Kohmura, *Phys. Rev. Lett.* **124**, 118004 (2020).
- [65] H. Eyring, *J. Chem. Phys.* **4**, 283 (1936).

- [66] H.-N. Lee, K. Paeng, S. F. Swallen, and M. D. Ediger, *Science* **323**, 231 (2009).
- [67] J. Rottler and M. O. Robbins, *Phys. Rev. E* **68**, 011507 (2003).
- [68] E. Bouchbinder and J. S. Langer, *Phys. Rev. E* **80**, 031133 (2009).
- [69] W. H. Wang, Y. Yang, T. G. Nieh, and C. T. Liu, *Intermetallics* **67**, 81 (2015).
- [70] K. Chen and K. S. Schweizer, *Europhys. Lett.* **79**, 26006 (2007).
- [71] K. Chen and K. S. Schweizer, *Phys. Rev. Lett.* **102**, 038301 (2009).
- [72] K. Chen and K. S. Schweizer, *Phys. Rev. E* **82**, 041804 (2010).
- [73] K. Chen and K. S. Schweizer, *Macromolecules* **44**, 3988 (2011).
- [74] R. S. Hoy and M. O. Robbins, *J. Polym. Sci. B Polym. Phys.* **44**, 3487 (2006).
- [75] R. S. Hoy and M. O. Robbins, *Phys. Rev. Lett.* **99**, 117801 (2007).
- [76] S. Plimpton, *J. Comput. Phys.* **117**, 1 (1995).
- [77] K. Dalnoki-Veress, J. A. Forrest, C. Murray, C. Gigault, and J. R. Dutcher, *Phys. Rev. E* **63**, 031801 (2001).
- [78] A. Shavit and R. A. Riggleman, *Macromolecules* **46**, 5044 (2013).
- [79] Y. Zhou, M. Freitag, J. Hone, C. Staii, A. T. Johnson Jr., N. J. Pinto, and A. G. MacDiarmid, *Appl. Phys. Lett.* **83**, 3800 (2003).
- [80] Y. Shi, J. Luo, F. Yuan, and L. Huang, *J. Appl. Phys.* **115**, 043528 (2014).
- [81] E. Y. Lin and R. A. Riggleman, *Soft Matter* **15**, 6589 (2019).
- [82] L. E. Govaert, T. A. P. Engels, M. Wendlandt, T. A. Tervoort, and U. W. Suter, *J. Polym. Sci. B Polym. Phys.* **46**, 2475 (2008).
- [83] I. H. Sahputra and A. T. Echtermeyer, *Model. Simul. Mater. Sci. Eng.* **21**, 065016 (2013).
- [84] V. M. Nazarychev, A. V. Lyulin, S. V. Larin, A. A. Gurtovenko, J. M. Kenny, and S. V. Lyulin, *Soft Matter* **12**, 3972 (2016).
- [85] S. Tu, X. Ren, J. He, and Z. Zhang, *Fatigue Fract. Eng. Mater. Struct.* **43**, 3 (2020).
- [86] T. Kwon and B. J. Sung, *Phys. Rev. E* **98**, 042503 (2018).
- [87] K. Kremer and G. S. Grest, *J. Chem. Phys.* **92**, 5057 (1990).
- [88] L. M. Nicholson, K. S. Whitley, T. S. Gates, and J. A. Hinkley, *J. Mater. Sci.* **35**, 6111 (2000).
- [89] G. J. Papakonstantopoulos, K. Yoshimoto, M. Doxastakis, P. F. Nealey, and J. J. de Pablo, *Phys. Rev. E* **72**, 031801 (2005).